coatings

MDPI

Article

The Effects of Surface Plasma Carburization on the Microstructure and Molten Salt Corrosion Resistance of Ta

Xuming Lv [1], Dongbo Wei [2,3,*], Xianpu Huang [2,3], Zeyu Gao [2,3] and Pingze Zhang [2,3]

[1] Science and Technology on Particle Transport and Separation Key National Defense Laboratory, Research Institute of Physical and Chemical Engineering of Nuclear Industry, Tianjin 300180, China; lvxuming2008@126.com
[2] College of Materials Science and Technology, Nanjing University of Aeronautics and Astronautics, Nanjing 210016, China; sx2306073_hxp@nuaa.edu.cn (X.H.); gaozeyu@nuaa.edu.cn (Z.G.); pzzhang@nuaa.edu.cn (P.Z.)
[3] Key Laboratory of Materials Preparation, Evaluation, and Application for Harsh Environment, MIIT (Ministry of Industry and Information Technology), Nanjing University of Aeronautics and Astronautics, Nanjing 210016, China
* Correspondence: weidongbo@nuaa.edu.cn

Abstract: In order to enhance the corrosion resistance of tantalum, the double-glow plasma (DGP) metallurgy technique was used to prepare TaC coatings on the tantalum. The morphology, microstructure, and phase constituents of TaC were examined by scanning electron microscopy (SEM) and X-ray diffraction (XRD). Nano-indentation tests were used to evaluate the mechanical properties of the coatings. The specimens were immersed in NaCl-KCl molten salt at 830 °C to evaluate their corrosion resistance. The results showed that the coating prepared by the DGP technique has a thickness of approximately 5 μm, the diffusion layer has a thickness of 2.5 μm, and the nano-indentation hardness is measured to be 17.27 GPa. The high-temperature stable ceramic phase enhances the high-temperature oxidation resistance of pure tantalum (Ta), while the dense corroded surface and oxidation products improve the anti-corrosion property of TaC coatings.

Keywords: Ta; plasma carburization; TaC coatings; microscopic structure; molten salt corrosion

Citation: Lv, X.; Wei, D.; Huang, X.; Gao, Z.; Zhang, P. The Effects of Surface Plasma Carburization on the Microstructure and Molten Salt Corrosion Resistance of Ta. *Coatings* **2024**, *14*, 1570. https://doi.org/10.3390/coatings14121570

Academic Editor: Alessandro Patelli

Received: 11 November 2024
Revised: 12 December 2024
Accepted: 13 December 2024
Published: 16 December 2024

1. Introduction

Tantalum (Ta), a refractory transition metal, is widely used in the aerospace, chemical engineering, and nuclear industries due to its high melting point (2996 °C), excellent processability, and corrosion resistance. However, uncoated tantalum has limitations such as relatively low hardness, inadequate scratch resistance, and poor wear resistance, restricting its use in high-wear applications [1–8]. Additionally, the highly reactive nature of tantalum makes it prone to oxidation in air, demonstrating poor resistance to high-temperature oxidation. The thin, dense, and stable oxide layer that forms on the surface of tantalum at room temperature begins to deteriorate above 300 °C, with the oxidation rate rapidly increasing at higher temperatures [9,10].

Tantalum carbide (TaC), as a refractory metal carbide, offers a much higher melting point (3880 °C), high hardness (13.5–20 GPa), and excellent resistance to chemical corrosion and oxidation, making it ideal for ultra-high temperature and corrosive environments [11–19]. However, due to its high hardness and brittleness, TaC is difficult to process into complex shapes; therefore, it is often used as a coating material. By subjecting tantalum to carburization modification, a carbonized layer can be formed on its surface, which effectively improves the wear resistance and oxidation resistance of the base material. For instance, Rubinshtein et al. and Raveh A et al. used a radio-frequency-induced plasma-assisted carburizing (IPCVD) method to produce a carburized layer of TaC and Ta_2C, finding that higher TaC content increased the hardness and corrosion resistance [20,21]. Chong et al. used vacuum carburizing technology to create TaC/Ta_2C carburized bilayer

films on Ta substrates, with hardness ranging from 14.632 to 35.832 GPa, depending on the carbon concentration in non-stoichiometric compounds, and found that the bilayer film effectively protected Ta from oxidation [22].

Current approaches for surface carbon infiltration to Ta include solid-state [23,24], gas [25,26], and ion diffusion [27,28]. Owing to its substantial metallic properties—dense, with a high melting point, and a robust passive layer—tantalum commonly required higher temperature of around 2000 °C to catalyze the carbon absorption process. Gas diffusion processes are slow, require a high temperature, and tend to result in uneven carbon layers, while solid-state diffusion constructs thick yet less dense layers. Techniques such as Chemical Vapor Deposition (CVD) and Pulsed Laser Deposition (PLD) often produce carbon layers with noticeable delineations at the coating–substrate junction, fostering setbacks in interfacial cohesion. In pursuit of fidelity in the coating's adhesion to its substrate, double-glow plasma carburizing technology has emerged as a promising method. This technique uses a hollow cathode effect, generated by the potential difference between two cathode plates in a vacuum, to achieve surface carbonization at relatively low temperatures compared to gas carburizing and solid carburizing. It offers robust interfacial adhesion, extensive applicability, and tunable layer composition, and avoids hydrogen embrittlement, making it ideal for enhancing Ta surface treatments [29–31].

In this study, we employed double-glow plasma metallurgical technology to carburize Ta substrates and produce TaC coatings. The composition and structure of the coatings were analyzed, and the corrosion behavior of the TaC coating in an 830 °C NaCl-KCl melt was investigated through immersion experiments.

2. Materials and Methods

The Ta substrate used in this study has a purity of 99.99% and dimensions of 15 mm × 15 mm × 4 mm (provided by Yuri Sheng Metal Co., Ltd., Qinghe, China). It was progressively ground and polished using metallographic sandpapers ranging from 200 to 8000 grit, followed by ultrasonic cleaning in anhydrous ethanol for 15 min, and then it was dried for future use. The purity of the graphite target (Tegas New Material Technology Co., Ltd., Shijiazhuang, China) material is 99.99%, with dimensions of Φ100 mm × 6 mm.

The double-glow plasma carburizing setup is illustrated in Figure 1. In this system, the graphite target serves as the source electrode (first cathode), providing the desired infiltration element, while the Ta substrate acts as the workpiece electrode (second cathode). The chamber wall is used as the anode, completing a closed circuit in the vacuum chamber. Each cathode is connected to a high-frequency DC pulse power supply (PI-10AH, China Nuclear Tongchuang technology Co., Ltd., Chengdu, China), supply frequency 43 kHz with 80% duty cycle. Argon (Ar) gas (purity 99.99%, flow rate of 100 sccm, Jiangsu Tianhong Chemical Co., Ltd., Wuxi, China) is introduced into the vacuum chamber, and when the predetermined pressure is reached, solely activating the workpiece voltage for 30 min, the purpose of surface activation and cleaning is achieved through the bombardment of the sample with high-energy particles. Subsequently, the source and cathode power supplies are connected separately to create a voltage difference between the sample and the target, producing a double-glow effect.

During this process, Ar ionization generates Ar^+ and electrons. The Ar^+ ions continuously bombard the target material (graphite) under the electric field, causing carbon atoms to sputter out to form high-energy particles (mainly composed of graphite clusters, atoms, and a small number of ions), and deposit onto the surface of the workpiece. Under the bombardment of particles, the temperature of the substrate continuously increases, promoting the infiltration of elements into the interior of the workpiece, forming a modified coating [32]. The thickness and microstructure of the coating can be controlled by adjusting process parameters such as voltage, pressure, and insulation time. The specific experimental parameters are detailed in Table 1.

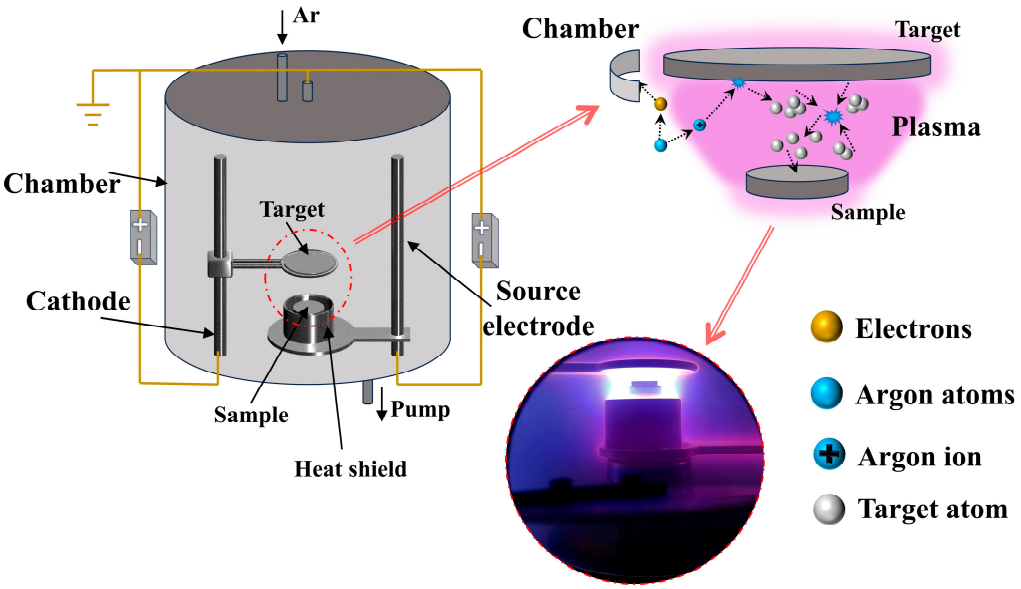

Figure 1. Schematic illustration of double-glow plasma surface carburizing technology producing TaC coatings on Ta surface.

Table 1. Experimental process parameters of double-glow plasma carburizing.

Items	Glow Discharge Sputtering
Processing temperature/°C	1000
Processing time/h	7.5
Working gas pressure/Pa	35
Distance between the target and substrate/mm	11

The surface and cross-sectional morphology, as well as the composition of the TaC coating before and after corrosion, were examined using a scanning electron microscope (SEM, Hitachi S-4800 Hitachi Limited, Tokyo, Japan). The phase composition of the TaC coating was determined by using X-ray diffraction (XRD, BrukerD8-ADVANCE, BRUKER AXS GMBH, Karlsruhe, Germany) using monochromatic Cu Kα radiation (λ = 1.5418 Å). The chemical composition and distribution of the TaC coating were analyzed with energy dispersive spectroscopy (EDS, TESCAN Group a. s., Brno, Czechia) automatic line scan. The Vickers microhardness of both the substrate and the alloy layer was measured using an HXS-1000AY micro-Vickers hardness tester (Nanjing Haote Technology Co, Nanjing, China), using a load of 100 g and a dwell time of 10 s. The nano-hardness and elastic modulus of the Ta matrix and infiltration layer were tested with a German Bruker Hysitron TI980 nano-indenter (Bruker Co, Billerica, MA, USA) equipped with a diamond right-angled triangular cone indenter. The maximum applied load was 100 mN, with a loading rate of 1.3239 mN/s and a dwell time of 15 s.

To investigate the high-temperature molten salt corrosion resistance of the TaC coating, an immersion corrosion test was performed using a molten salt method. The results from SEM, EDS, and XRD analyses were used for corrosion evaluation. The corrosive medium used was an equimolar NaCl-KCl molten salt at 830 °C, and the test was conducted in an air atmosphere. Before the corrosion test, the specimen was embedded in a mixture of NaCl-KCl salts, and heated to 300 °C using a KSL-1100X-type high-temperature resistance furnace (Hefei Kejing Material Technology Co., Ltd., Hefei, China) at a heating rate of 10 °C/min, held for 2 h to remove any bound water from the mixture of salts. Subsequently, the specimen was further heated to 830 °C along with the molten salt and was held at this temperature, and the corrosion experiment was initiated. The samples were immersed for 1 h, 4 h, and 7 h at 830 °C, respectively, with temperature control accuracy of ±1 °C. After the corrosion process, the samples were air-cooled to room temperature and cleaned in

boiling water (distilled water) three to five times to remove any residual salt and corrosion products. All the samples were then ultrasonically cleaned in anhydrous ethanol for 15 min, followed by vacuum drying and weighing multiple times to obtain an average value. The NaCl (99.5%) and KCl (99.5%) used in the experiment were sourced from Nanjing Chemical Reagent Co., Ltd. Weighing was performed using an electronic scale (FA2004, Shanghai Sunny Hengping Scientific Instrument Co., Ltd., Shanghai, China) with a precision of 0.1 mg.

3. Results and Discussion

3.1. Microstructure of TaC Coatings

The morphology and composition of the infiltration layer are shown in Figure 2. The surface of the TaC infiltration layer (Figure 2a) is densely packed and smooth, with no apparent defects such as holes. Alloy elements aggregated and grew to form small-sized TaC particles on the surface. The carbon content on the surface is 10.3% by mass, with a molar fraction of approximately 65.99%, distributed uniformly without signs of elemental agglomeration. Figure 2b presents the XRD pattern of the TaC coating layer, where the diffraction peaks of the body-centered cubic (BCC) Ta disappear after the carburizing process, and are replaced by new diffraction peaks. The dominant phase is face-centered cubic (FCC) TaC, and no free graphite phase is detected.

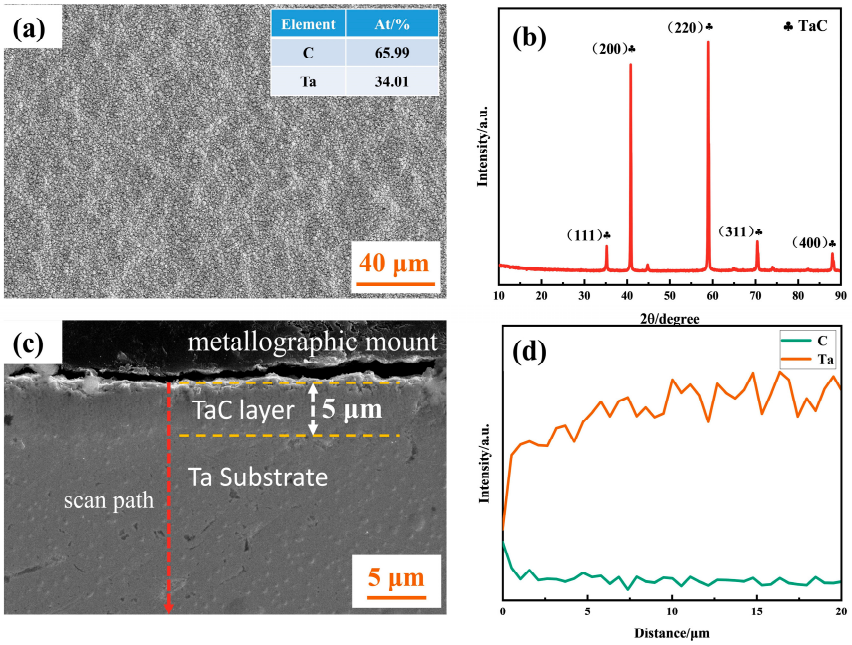

Figure 2. Surface SEM (**a**) and cross-section SEM (**c**) and XRD (**b**), EDS (**d**) analysis of carburization layer.

The analysis of the cross-sectional morphology (Figure 2c) and the energy dispersive spectroscopy (EDS) automatic line scan one-minute of elemental distribution chart (Figure 2d) reveals that the cross-section of the infiltration layer is uniform and dense, without structural defects such as pores, cracks, and inclusions. There is a diffusion distribution of elements at the interface with the substrate, with no distinct boundary line. The outermost layer is the TaC coating, with grains showing a columnar growth characteristic and a thickness of approximately 5 μm (μm). The inner part is the element inter-diffusion zone between the TaC coating and the substrate, tightly bonded to the substrate. From the TaC coating to the substrate, the content of the C element gradually decreases while the Ta element content gradually increases. The transition of the composition gradient between the TaC infiltration layer and the substrate can effectively enhance the bonding between the layer and the substrate, ensuring the working stability and service life of the alloy layer.

3.2. Mechanical Properties

All the fabricated samples were analyzed for their mechanical properties, and the results are summarized in Table 2. For more reliable data, five individual values were collected from different points of each sample and their average values were taken as standard ones. The average micro-Vickers hardness of the Ta matrix surface is 121.42 $HV_{0.1}$. After the formation of the carburizing layer on its surface, the average hardness of the formed TaC layer is approximately 1615.66 $HV_{0.1}$—about 13 times higher than that of the original Ta matrix. This substantial hardness increase is primarily due to the successful formation of the TaC phase, as surface Ta reacts with the C during the carburizing process. As a type of ceramic carbide, TaC inherently possesses high hardness. Additionally, free C atoms diffuse into the interstitial sites of the Ta and TaC crystal lattices during the double halide carburizing process. This diffusion contributes to solid solution strengthening, and fills in some defects within the coating, which explains the remarkable hardness of the carburized layer on the Ta surface.

Table 2. Experimental process parameters of double-glow plasma carburizing.

Points	1	2	3	4	5	Average ($HV_{0.1}$)
Ta	118.0	122.4	117.2	131.2	118.3	121.42
TaC	1658.2	1546.6	1532.8	1652.3	1688.4	1615.66

The microhardness and elastic modulus of both the Ta matrix and the TaC diffusion layer were tested using the nano-indentation method, as shown in Figure 3. The load-displacement curves for the Ta matrix and the TaC diffusion layer did not exhibit step-like changes (Figure 3a), indicating a smooth transition, which suggests good toughness during loading and unloading without stress concentration. The Ta matrix exhibited a nano-hardness of 1.87 GPa and an elastic modulus of 176.73 GPa. In contrast, the TaC diffusion layer demonstrated significantly higher mechanical properties, with a nano-hardness of 17.27 GPa and an elastic modulus of 302.92 GPa. The hardness of the TaC layer increased by approximately 9.26 times, and its elastic modulus reached 171% of that of the Ta matrix.

The H/E and H^3/E^2 ratios reflect the material's surface contact limit and resistance to plastic deformation, as shown in Figure 3c. The H/E ratios for the Ta matrix and the TaC diffusion layer were 1.06×10^{-2} and 5.70×10^{-2}, and the H^3/E^2 values were 2.08×10^{-4} and 5.61×10^{-2}, respectively. This indicates that the surface contact limit of the TaC diffusion layer is about five times higher, and its resistance to plastic deformation is two orders of magnitude higher than the Ta matrix. These improvements in the surface properties of the carburized TaC diffusion layer significantly contribute to enhancing the service life of the Ta matrix.

The ratio of elastic to plastic work (K) is indicative of a material's load-bearing capacity, with higher K values representing greater strength. In the TaC diffusion layer, the elastic work increased from 3.95×10^{-9} J in the Ta matrix to 7.65×10^{-9} J, while the plastic work decreased from 5.69×10^{-8} J in the Ta matrix to 9.72×10^{-9} J (Figure 3d). The calculated K values for the Ta matrix and the TaC diffusion layer were 0.07 and 0.79, respectively, highlighting a much higher load-bearing capacity for the TaC diffusion layer, which is attributed to the excellent mechanical properties of the surface-formed TaC ceramic phase.

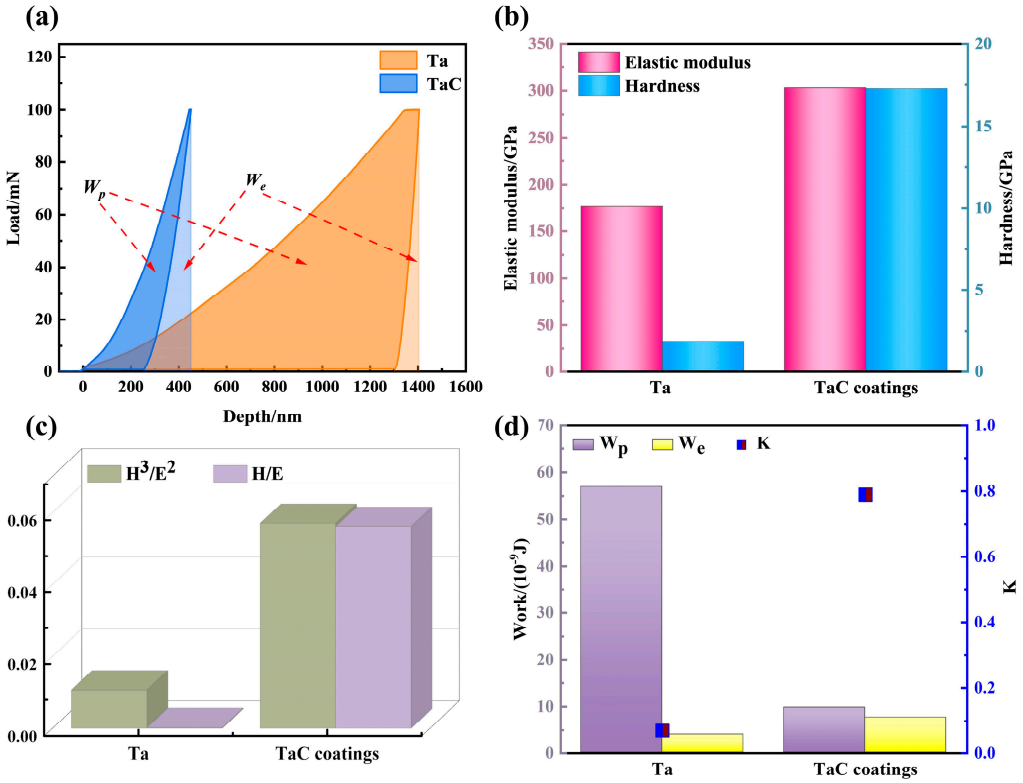

Figure 3. Mechanical properties of the Ta matrix and TaC carburized coating layer. (**a**) Load-displacement curves; (**b**) nano-hardness and elastic modulus; (**c**) H/E and H^3/E^2 ratios; (**d**) elastic work (W_e), plastic work (W_p), and their ratio (K).

3.3. Corrosion Results

To investigate corrosion products and their evolution during molten salt corrosion, XRD analysis was conducted on samples exposed to corrosion for three distinct time periods. Figure 4 displays the XRD spectra of the Ta matrix and the TaC infiltration layer after 1, 4, and 7 h of corrosion in NaCl-KCl molten salt at 830 °C. It is evident that the main corrosion products for Ta are compounds of Na-Ta-O (including $NaTaO_3$ and $Na_2Ta_4O_{11}$), with traces of Ta_2O_5. In the TaC infusion layer, the main corrosion products are $NaTaO_3$ and $Na_2Ta_4O_{11}$.

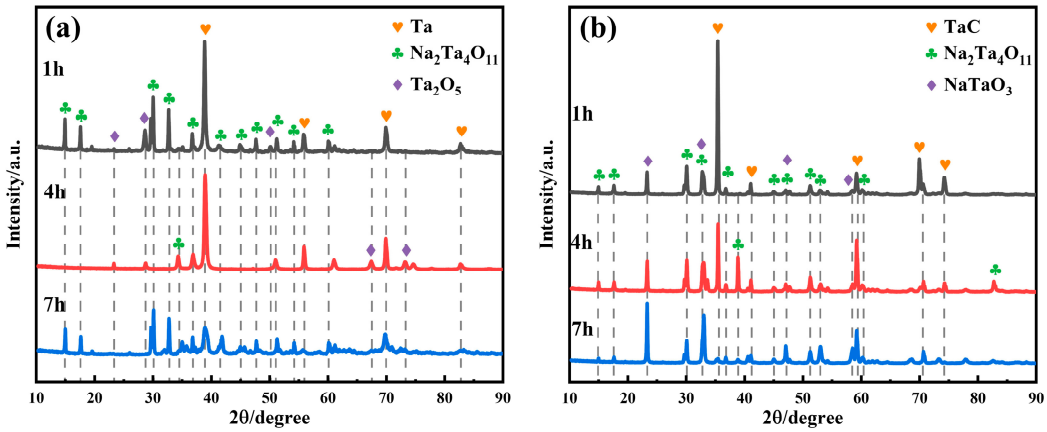

Figure 4. XRD pattern of Ta (**a**) and TaC (**b**) coatings after molten salt corrosion.

During the initial stage of corrosion, the surface of the Ta matrix primarily consists of Ta with FCC structure, and compounds formed from the reaction of Ta with the molten

salts ((Na,K)-Ta-O) [33–35]. As shown in Figure 4a, these compounds are predominantly $Na_2Ta_4O_{11}$ and some $NaTaO_3$. As corrosion reactions progress, the diffraction peak intensities of Ta decrease, matching precisely with those of $Na_2Ta_4O_{11}$ and $NaTaO_3$.

In the case of the TaC layer, after the first hour of corrosion, the diffraction peak intensity for TaC remains high, with remaining smaller peaks corresponding to $NaTaO_3$ and $Na_2Ta_4O_{11}$, indicating minimal corrosion and good preservation of the infiltration layer. By the fourth and seventh hour of corrosion, while the types of corrosion products remain the same, the intensities of the diffraction peaks vary. As the duration of corrosion extends, TaC increasingly reacts with the molten salts, leading to increased corrosion and the formation of increasing amounts of Na-Ta-O compounds. Notably, the diffraction peak intensity of $NaTaO_3$ increased significantly, suggesting some conversion of $Na_2Ta_4O_{11}$ into $NaTaO_3$ over time.

The corrosion behavior of the untreated and surface-carburized Ta specimens in NaCl-KCl melts at 830 °C as a function of immersion time is shown in Figure 5. It can be easily observed that the weight loss of the carburized specimen is lower than that of the untreated Ta specimen, and the trend of increasing and then decreasing the weight of the Ta specimen is caused by the formation and shedding of the oxide layer.

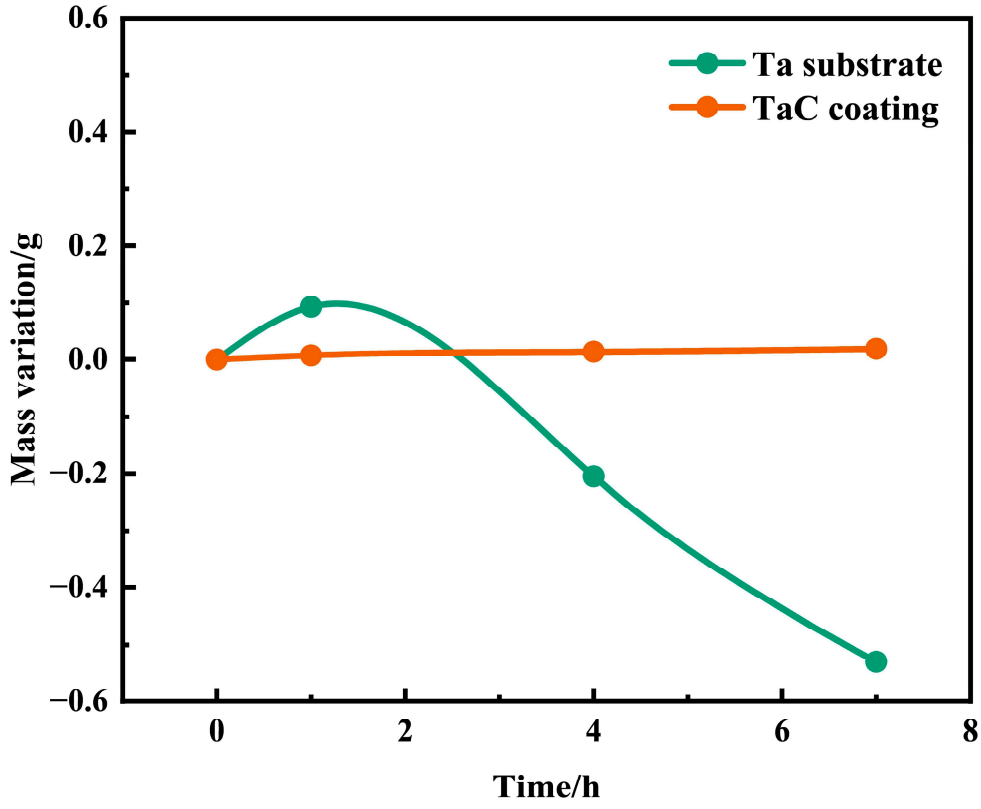

Figure 5. Corrosion kinetics of TaC coatings and untreated Ta in NaCl-KCl melts.

SEM analysis was employed to investigate the surface morphology and elemental composition of the Ta matrix and TaC infiltration layer after molten salt corrosion for 1, 4, and 7 h, with varying magnifications as shown in Figure 6. The surface of the Ta matrix displayed innumerable rod-shaped corrosion products growing in the form of strips with micro-cracks forming between them. The elemental analysis revealed lower concentrations of K and Cl compared to Na, aligning with the XRD results, where the Cl element was almost undetectable. It is hypothesized that during the molten salt corrosion, Cl_2 gas was produced and released into the atmosphere, reducing the Cl content. Combining the XRD results, the main corrosion products were identified as Na-Ta-O compounds, particularly $Na_2Ta_4O_{11}$. Additionally, the corrosion products formed aggregations with

a porous structure, leading to the formation of holes after the corrosion layer peeled off. This served as a pathway for Na and O atoms to penetrate deeper and further corrode the internal structure, accelerating the degradation of the Ta matrix. After 7 h of corrosion, the surface displayed bright regions (Area A) and dark regions (Area B), as depicted in Figure 6a2. Elemental analysis confirmed that Area A was part of the corrosion layer, consisting of a Na-Ta-O compounds, while Area B was mainly exposed Ta, where the corrosion layer had peeled off. An increase in the corrosion layer's thickness caused stress concentration, leading to significant peeling phenomena.

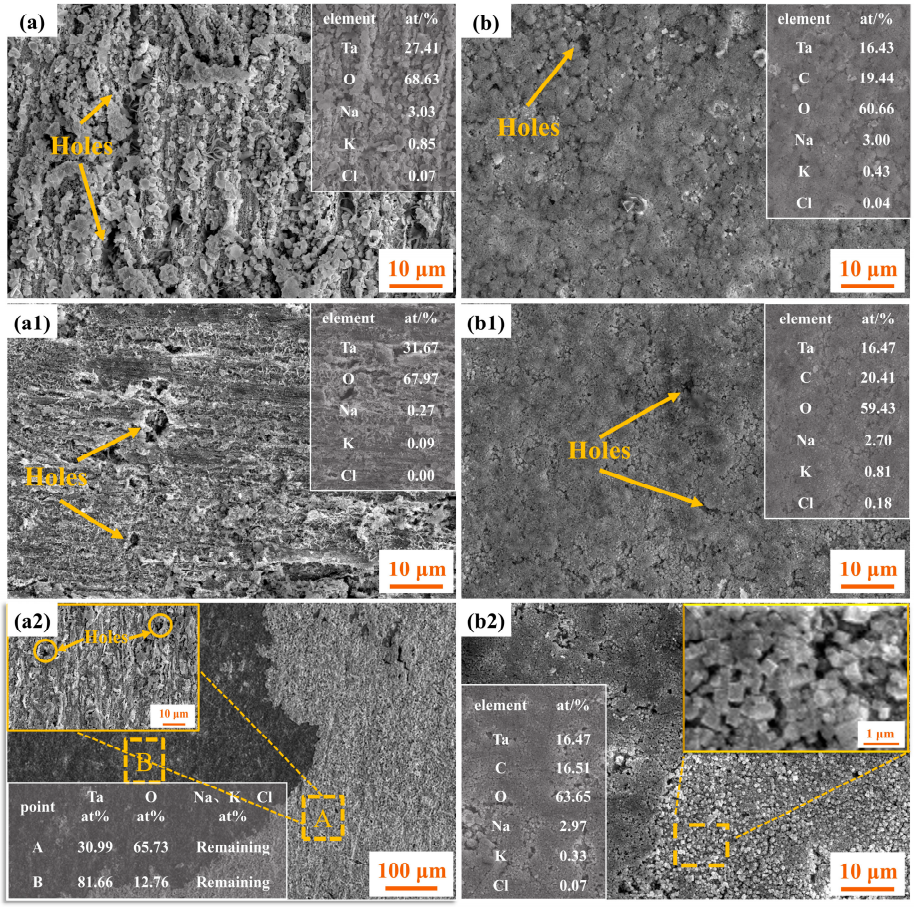

Figure 6. Surface morphologies of the Ta and TaC infiltration layers after molten salt corrosion. (**a**–**a2**) Ta 1 h, 4 h, 7 h; (**b**–**b2**) TaC 1 h, 4 h, 7 h.

In contrast, the TaC infiltration layer displayed a smoother surface after corrosion, with more densely packed corrosion products, fewer aggregations, and fewer cracks and holes, compared to the Ta matrix. The significant reduction in the surface content of C was attributed to the reaction of surface TaC and minor graphite with the high-temperature chlorine salts, releasing CO_2. This CO_2 could have further reacted to form Na_2CO_3 or K_2CO_3, subsequently forming a mixed salt with NaCl-KCl and being dissolved and removed during ultrasonic cleaning. After 7 h of corrosion, the number of corrosion products and surface holes increased, and prolonged corrosion led to micro-peeling, exposing granulated Na-Ta-O compounds. Upon further examination, these compounds revealed themselves as cubic crystals with various regular shapes, as shown in Figure 6b2. This granulation resulted from directional growth of crystals, with different morphologies observed, such as square, cubic, and multi-faceted polyhedral blocks, identified as $NaTaO_3$, while flaky, rod-like, and hexagonal blocky particles were identified as $Na_2Ta_4O_{11}$ [36].

The cross-sectional morphology and elemental line scan results of samples subjected to molten salt corrosion at 830 °C for 1, 4, and 7 h are illustrated in Figure 7. During

the preparation of the cross-sectional samples, fractures occurred in the loosely packed corrosion layer due to stress. The elemental line scan revealed that after 1 h of corrosion (Figure 7a), the corrosion layer was about 9 µm thick; however, oxygen diffused to a depth of 12 µm into the substrate. After 4 and 7 h of corrosion (Figure 7b,c), the thickness of the corrosion layer increased to around 12 µm. The corrosion behavior of the Ta matrix followed a "corrosion–peeling–re-corrosion" cycle. Once the corrosion layer reached a certain thickness, the internal stress, driven by the interaction of hot molten salts and oxygen, weakened its attachment to the Ta matrix, resulting in breakage and delamination. This led to substantial material damage and mass loss. The recurring corrosion exposed fresh Ta surfaces to the corrosive medium, promoting further corrosion. The existing layer struggled to prevent the penetration of elements like sodium and oxygen, leading to the breakdown of the Ta matrix.

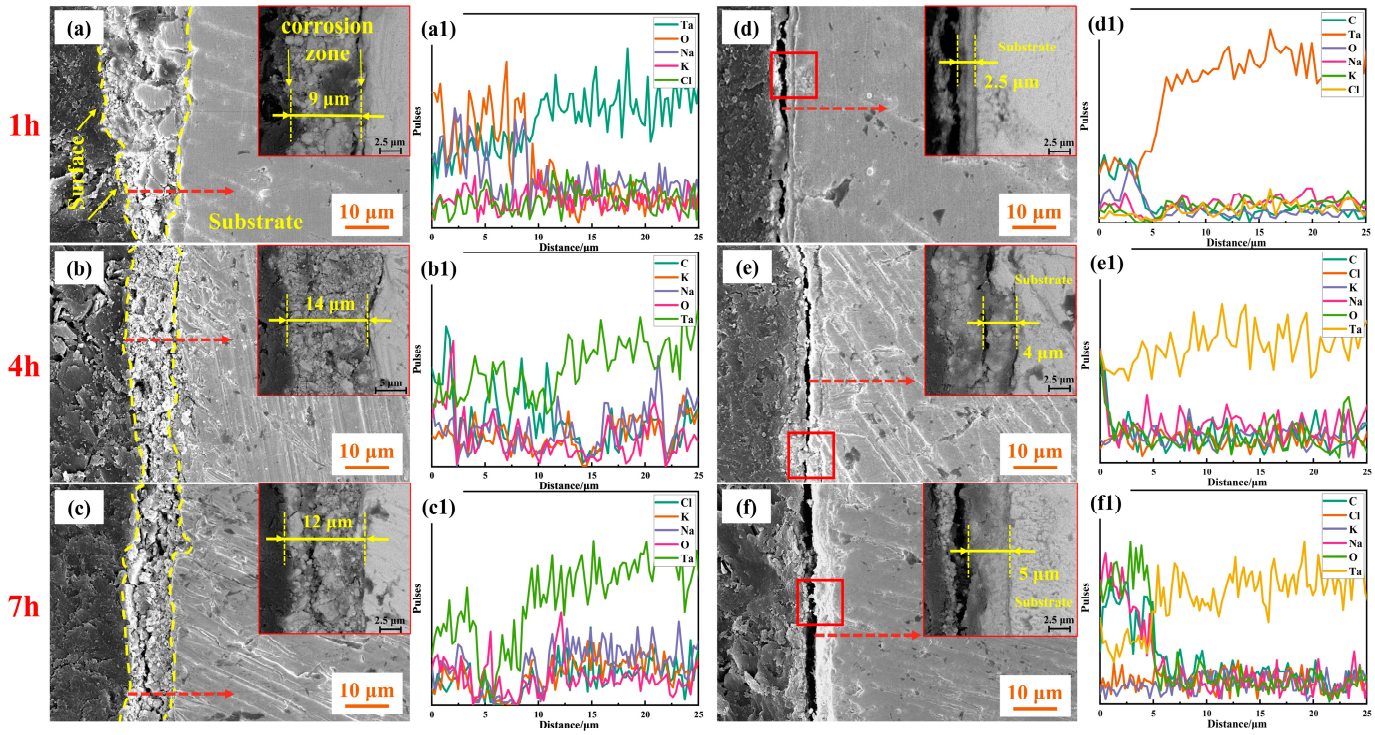

Figure 7. Cross-sectional morphology and elemental line scan of Ta matrix after molten salt corrosion for (**a**,**a1**) 1 h, (**b**,**b1**) 4 h, and (**c**,**c1**) 7 h, respectively. Cross-sectional morphology and elemental line scan of TaC infiltration layer after molten salt corrosion for (**d**,**d1**) 1 h, (**e**,**e1**) 4 h, and (**f**,**f1**) 7 h, respectively.

In contrast, surface carburization eliminated the fragmentation seen in the Ta matrix's corrosion layer. The layer formed on the carburized surface was more tightly packed, continuous, and well-bonded. Also, the thickness of this layer increased with prolonged corrosion duration. The TaC layer maintained a thickness of around 2.5 µm (Figure 7d), with a diffusion zone of about 2.5 µm beneath it. The corrosion of the TaC layer progressed more slowly, effectively postponing the seepage of elements such as sodium, potassium, and oxygen, thereby protecting the Ta matrix from internal corrosion. After enduring 7 h of corrosion, a noticeable increase in the content of sodium and oxygen elements on the surface was observed, correlating with the production of a considerable number of Na-Ta-O compounds. The carbon diffused outward under high temperatures, reacting with the molten NaCl-KCl salts, causing the corrosion layer to thicken to approximately 5 to 6 µm (Figure 7f). At this stage, the diffusion zone was not fully depleted, continuing to slow the inward progression of corrosion and diminishing its overall severity.

Based on XRD and SEM-EDS analysis of corrosion caused by NaCl-KCl molten salts over different durations, a schematic diagram illustrates the changes on the TaC coating surface (Figure 8). When tantalum is exposed to molten chloride salts, it reacts with oxygen and chloride ions to produce Ta_2O_5 and Na-Ta-O compounds, while also releasing chlorine gas. The significant mismatch in thermal expansion coefficients and distinct crystal structures between Na-Ta-O and Ta_2O_5 leads to increased internal stress, leading to surface cracks and eventually peeling off. However, after carbon infiltration into the surface, the Ta substrate is protected. Unlike Ta, which has a Gibbs free energy of −64 kJ, TaC is more stable at high temperatures, with a Gibbs free energy of −221 kJ, making it less reactive [37]. The infiltrated TaC layer offers a degree of insulation between the Ta substrate and high-temperature molten salts, reducing the depth of the corrosive medium and easing the volumetric expansion issues between Na-Ta-O compounds and the Ta substrate. Furthermore, carbon has a higher affinity for oxygen than Ta; small amounts of free graphene on the surface and carbon within the TaC preferentially react with the O_2 available in the molten salts, producing CO and CO_2 gases, thereby reducing the partial pressure of oxygen, which in turn limits the formation of other corrosive agents like Cl_2. Additionally, the high-temperature-driven diffusion of carbon towards the corroded surface also facilitates the reaction between carbon and oxygen. Consequently, the TaC layer effectively impedes the corrosive agents from attacking the un-corroded film and substrate, providing enhanced protection.

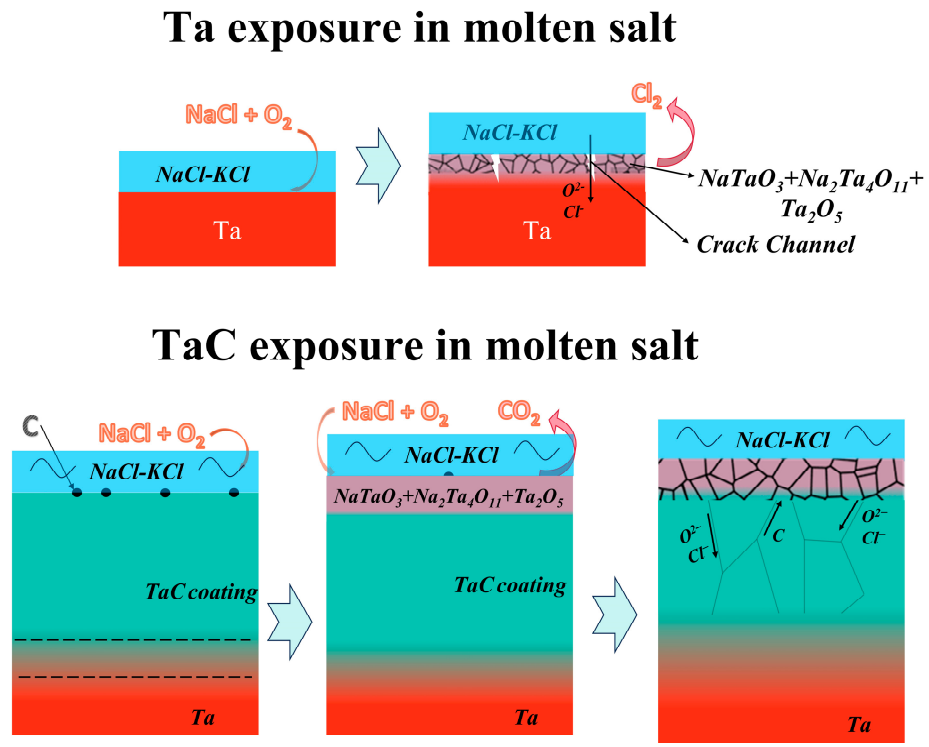

Figure 8. Schematic illustration of corrosion behaviors of Ta and TaC coatings in NaCl-KCl molten salt.

4. Conclusions

1. A TaC diffusion layer was formed on the surface of pure tantalum using a double-glow plasma carburizing technique. The grains in the TaC diffusion layer exhibit columnar growth and are metallurgically bonded to the substrate. The surface of the carburized layer is dense, smooth, and free from pores or other defects. The diffusion layer primarily consists of the TaC phase, with almost no free graphite phase present. The elemental content within the diffusion layer is distributed in a gradient, with no obvious boundary line between the diffusion layer and the substrate.

2. The preparation of the TaC diffusion layer using the double-glow discharge carburizing technique significantly improves the hardness and elastic modulus of pure tantalum material. The surface hardness of the material increases from 121.42 $HV_{0.1}$ to 1615.66 $HV_{0.1}$, while the nano-hardness rises from 1.87 GPa to 17.27 GPa, and the elastic modulus improves from 176.73 GPa to 302.92 GPa.
3. The corrosion of tantalum treated with surface carburization occurs entirely within the TaC layer, with the corrosion layer mainly composed of $NaTaO_3$ and $Na_2Ta_4O_{11}$. Due to the excellent thermodynamic stability of TaC and its effective protective role in maintaining the surface corrosion layer, the corrosion rate of the TaC coating is slow, significantly enhancing the tantalum's resistance to thermal corrosion in molten salts at elevated temperatures.

Author Contributions: Conceptualization, X.L. and D.W.; formal analysis, X.H. and Z.G.; software, X.H. and Z.G.; investigation, Z.G.; data curation, Z.G. and X.H.; resources, P.Z., X.L. and D.W.; validation, Z.G. and X.H.; writing—original draft, X.H.; writing—review and editing, X.H. and D.W.; visualization, X.H. and Z.G.; supervision, D.W. and P.Z.; project administration, D.W. and X.L.; funding acquisition, D.W., X.L. and P.Z. All authors have read and agreed to the published version of the manuscript.

Funding: This research is supported by open Project Research Funds for Science and Technology on Particle Transport and Separation Key National Defense Laboratory (2022-JCJQ-LB-004).

Institutional Review Board Statement: Not applicable.

Informed Consent Statement: Not applicable.

Data Availability Statement: Data are contained within the article.

Conflicts of Interest: The authors declare no conflict of interest.

References

1. Lim, J.-W.; Ishikawa, Y.; Miyake, K.; Yamashita, M.; Isshiki, M. Improvement of Ta Barrier Film Properties in Cu Interconnection by Using a Non-mass Separated Ion Beam Deposition Method. *Mater. Trans.* **2002**, *43*, 478–481. [CrossRef]
2. Laurila, T.; Zeng, K.; Kivilahti, J.K.; Molarius, J.; Riekkinen, T.; Suni, I. Tantalum carbide and nitride diffusion barriers for Cu metallisation. *Microelectron. Eng.* **2002**, *60*, 71–80. [CrossRef]
3. Brady, M.P.; Zhu, J.H.; Liu, C.T.; Tortorelli, P.F.; Walker, L.R.; McKamey, C.G.; Wright, J.L.; Carmichael, C.A.; Larson, D.J.; Miller, M.K.; et al. Intermetallic reinforced Cr alloys for high-temperature use. *Mater. High Temp.* **1999**, *16*, 189. [CrossRef]
4. Wang, D.F.; Liaw, P.K.; Liu, C.T.; George, E.P. Processing and Microstructure of Cr-Ta and Cr-Ta-Mo Composites Reinforced by the Cr2Ta Laves Phase. In Proceedings of the 17th Annual Conference on Fossil Energy Materials, Baltimore, MD, USA, 29 July 2002. [CrossRef]
5. Brant, C.L. New applications and novel processing of refractory metal alloys. *Met. Powder Rep.* **2002**, *57*, 40. [CrossRef]
6. He, Y.H.; Liaw, P.K.; Lu, Y.; Liu, C.T.; Heatherly, L.; George, E.P. Effects of processing on the microstructure and mechanical behavior of binary Cr–Ta alloys. *Mater. Sci. Eng. A* **2002**, *329–331*, 696–702. [CrossRef]
7. Laurila, T.; Zeng, K.; Kivilahti, J.K.; Molarius, J.; Suni, I. Chemical stability of Ta diffusion barrier between Cu and Si. *Thin Solid Film.* **2000**, *373*, 64–67. [CrossRef]
8. Cotton, D.; Jacquet, P.; Faure, S.; Vignal, V. Ta_2C precipitation after low pressure carburizing of tantalum. *Mater. Chem. Phys.* **2022**, *278*, 125632. [CrossRef]
9. Kofstad, P. The Oxidation Behavior of Tantalum at 700°–1000°C. *J. Electrochem. Soc.* **1963**, *110*, 491. [CrossRef]
10. Voitovich, V.B.; Lavrenko, V.A.; Adejev, V.M.; Golovko, E.I. High-temperature oxidation of tantalum of different purity. *Oxid. Met.* **1995**, *43*, 509–526. [CrossRef]
11. Liu, L.; Ye, F.; Zhou, Y. New route to densify tantalum carbide at 1400 °C by spark plasma sintering. *Mater. Sci. Eng. A Struct. Mater. Prop. Microstruct. Process.* **2011**, *528*, 4710–4714. [CrossRef]
12. Chen, S.; Hu, H.; Zhang, Y.; Zhang, C.; Wang, Q. Effects of TaC amount on the properties of 2D C/SiC-TaC composites prepared via precursor infiltration and pyrolysis. *Mater. Des.* **2013**, *51*, 19–24. [CrossRef]
13. Liu, H.; Liu, L.; Ye, F.; Zhang, Z.; Zhou, Y. Microstructure and mechanical properties of the spark plasma sintered TaC/SiC composites: Effects of sintering temperatures. *J. Eur. Ceram. Soc.* **2012**, *32*, 3617–3625. [CrossRef]
14. Chen, Z.K.; Xiong, X.; Long, Y. Influence of TaCl 5 partial pressure on texture structure of TaC coating deposited by chemical vapor deposition. *Appl. Surf. Sci.* **2011**, *257*, 4044–4050. [CrossRef]
15. Zhang, X.; Hilmas, G.E.; Fahrenholtz, W.G. Densification and mechanical properties of TaC-based ceramics. *Mater. Sci. Eng. A Struct. Mater. Prop. Microstruct. Process.* **2009**, *501*, 37–43. [CrossRef]

16. Ahlén, N.; Johnsson, M.; Nygren, M. Oxidation behaviour of $Ta_xTi_{1-x}C$ and $Ta_xTi_{1-x}C_yN_{1-y}$ whiskers. *Thermochim. Acta* **1999**, *336*, 111–120. [CrossRef]
17. Barna, Á.; Kotis, L.; Pécz, B.; Sulyok, A.; Sáfrán, G.; Tóth, A.L.; Menyhárd, M.; Kovács, A.; Savenko, A. Thin TaC layer produced by ion mixing. *Surf. Coat. Technol.* **2012**, *206*, 3917–3922. [CrossRef]
18. Sciti, D.; Silvestroni, L.; Guicciardi, S.; Fabbriche, D.D.; Bellosi, A. Processing, mechanical properties and oxidation behavior of TaC and HfC composites containing 15 vol% TaSi2 or MoSi2. *J. Mater. Res.* **2009**, *24*, 2056–2065. [CrossRef]
19. Yang, K.; Chen, X.; Dang, B.; Wang, Y.; Jia, X.; Lu, F.; Li, S.; Zhang, P. Ablation behavior of Ta, TaC and Ta/TaC coatings on graphite under high-energy laser irradiation. *J. Mater. Sci.* **2024**, *59*, 11177–11192. [CrossRef]
20. Rubinshtein, A.; Shneck, R.; Danon, A.; Hayon, J.; Nathan, S.; Raveh, A. Surface treatment of tantalum to improve its corrosion resistance. *Mater. Sci. Eng. A* **2001**, *302*, 128–134. [CrossRef]
21. Raveh, A.; Danon, A.; Hayon, J.; Rubinshtein, A.; Shneck, R.; Klemberg-Sapieha, J.E.; Martinu, L. Characterization of carburized tantalum layers prepared in inductive RF plasma. *Thin Solid Film.* **2001**, *392*, 56–64. [CrossRef]
22. Di, C.; Yan, X.; Yang, Y.; Ye, W.; Zhao, M.; Li, D. Wear behaviors and high-temperature oxidation resistance properties of tantalum carbide layer. *Ceram. Int.* **2021**, *47*, 32766–32774. [CrossRef]
23. Zhao, Z.; Hui, P.; Liu, F.; Wang, X.; Li, B.; Xu, Y.; Zhong, L.; Zhao, M. Fabrication of TaC coating on tantalum by interstitial carburization. *J. Alloys Compd.* **2019**, *790*, 189–196. [CrossRef]
24. Matoba, T.; Nakase, E.; Sakaba, A. On Carburization of Tantalum Oxide. *J. Jpn. Soc. Powder Powder Metall.* **1965**, *12*, 69–77. [CrossRef]
25. Chrysanthou, A.; Grieveson, P. The behaviour of tantalum in the presence of CO and CO/CO_2 mixtures at elevated temperatures. *Mater. Sci. Eng. A Struct. Mater. Prop. Microstruct. Process.* **1995**, *194*, L11–L14. [CrossRef]
26. Di, C.; Yan, X.; Lv, X.; Yan, C.; Ye, W.; Li, D. Effect of Vacuum Carburizing Time on Microstructure and Mechanical Properties of Tantalum Carbide Layer. *Met. Mater. Int.* **2021**, *27*, 5008–5016. [CrossRef]
27. Nyberg, H.; Tokoroyama, T.; Wiklund, U.; Jacobson, S. Design of low-friction PVD coating systems with enhanced running-in performance—carbon overcoats on TaC/aC coatings. *Surf. Coat. Technol.* **2013**, *222*, 48–54. [CrossRef]
28. Nunogaki, M.; Inoue, M.; Yamamoto, T. Ceramic layers formed on metals by reactive plasma processing. *J. Eur. Ceram. Soc.* **2002**, *22*, 2537–2541. [CrossRef]
29. Xu, Z.; Xiong, F.F. Double Glow Discharge Phenomenon and Its Applications. In *Plasma Surface Metallurgy: With Double Glow Discharge Technology-Xu-Tec Process*; Xu, Z., Ed.; Springer: Singapore; Beijing, China, 2017; ISBN 978-981-10-5724-3.
30. Wei, D.; Gao, Z.; Lv, X.; Liu, J.; Zhang, P. Study on the structure, growth pattern and corrosion behavior of CoCrFeNiAl high entropy alloy coatings-base on hollow cathode effect. *Surf. Coat. Technol.* **2024**, *487*, 130967. [CrossRef]
31. Ni, R.; Wu, H.; Fan, Z.; Wei, Y.; Yu, L.; Jiang, F. Effect of Nb–Zr–N Alloying Layer on Surface Mechanical Properties and Biocompatibility of Medical 316L Matrix. *Coatings* **2023**, *13*, 1346. [CrossRef]
32. Wei, X.; Zhang, P.; Wei, D.; Zhao, H.; Wang, C.; Liskiewicz, T. Mechanical and tribological properties of Cr–Nb double-glow plasma coatings deposited on Ti–Al alloy. *Tribology* **2017**, *11*, 98–106. [CrossRef]
33. Suzuki, S.; Teshima, K.; Yubuta, K.; Ito, S.; Moriya, Y.; Takata, T.; Shishido, T.; Domen, K.; Oishi, S. Direct fabrication and nitridation of a high-quality $NaTaO_3$ crystal layer onto a tantalum substrate. *CrystEngComm* **2012**, *14*, 7178–7183. [CrossRef]
34. McLamb, N.; Sahoo, P.P.; Fuoco, L.; Maggard, P.A. Flux Growth of Single-Crystal $Na_2Ta_4O_{11}$ Particles and their Photocatalytic Hydrogen Production. *Cryst. Growth Des.* **2013**, *13*, 2322–2326. [CrossRef]
35. Zhang, M.; Liu, G.; Zhang, D.; Chen, Y.; Wen, S.; Ruan, S. Facile fabrication of NaTaO3 film and its photoelectric properties. *J. Alloys Compd.* **2014**, *602*, 322–325. [CrossRef]
36. Hu, K.; Hu, S.; Zeng, S.; Peng, B.; Xiong, X.; Wang, W.; Cheng, G. The effect of surface treatment on the corrosion behavior of pure Ta sheet in an equimolar NaCl-KCl melt at 850 °C in air, part 2: Diamond film, TaC film, Ta-Si coating and Ta-Si-Al coating. *Corros. Sci.* **2019**, *154*, 11–27. [CrossRef]
37. Bale, C.; Bélisle, E.; Chartrand, P.; Decterov, S.; Eriksson, G.; Hack, K.; Jung, I.-H.; Kang, Y.-B.; Melançon, J.; Pelton, A.; et al. Factsage Thermochemical Software and Databases—Recent Developments. *Calphad* **2009**, *33*, 295–311. [CrossRef]